2016-05-13

Focusing of baroclinic tidal energy in a canyon

Vlasenko, V

10.1002/2015JC011314
Journal of Geophysical Research: Oceans
American Geophysical Union (AGU)

Focusing of baroclinic tidal energy in a canyon

Vasiliy Vlasenko,[1] Nataliya Stashchuk,[1] Mark E. Inall,[2] Marie Porter,[2] and Dmitry Aleynik[2]

Corresponding author: V. VLasenko, School of Marine Science and Engineering, University of Plymouth, Drake Circus, Plymouth, PL4 8AA, UK. (vvlasenko@plymouth.ac.uk)

[1]School of Marine Science and Engineering, University of Plymouth, UK.

[2]Scottish Association for Marine Science, Scottish Marine Institute, Oban, UK.

Abstract.

Key points: Generation of internal tide in a circular canyon; Focusing of baroclinic tidal energy in the canyon centre; Generation of a baroclinic eddy due to diapicnal mixing.

Strong three dimensional focusing of internal tidal energy in the Petite Sole Canyon in the Celtic Sea is analysed using observational data and numerical modelling. In a deep layer (500-800 m) in the centre of the canyon shear variance was elevated by an order of magnitude. Corresponding large vertical oscillations of deep isotherms, and a local maximum of horizontal velocity were replicated numerically using the MITgcm. The elevated internal tidal activity in the deep part of the canyon is explained in terms of the downward propagation and focusing of multiple internal tidal beams generated at the shelf break. The near-circular shape of the canyon head and steep bottom topography throughout the canyon (steeper than the tidal beam) create favourable conditions for the lens-like focusing of tidal energy in the canyon's centre. Observations and modeling show that the energy focusing greatly intensifies local diapycnal mixing, that leads to local formation of a baroclinic eddy.

1. Introduction

Oceanic canyons are potential places for significant tidal energy conversion from the barotropic to baroclinic modes, with major implications for water mass mixing. According to *Hickey* [1995], nearly 20% of the Eastern Pacific shelf edge between Alaska and the equator is dominated by steep, narrow, and abrupt canyons. Historically, the first and most extensively studied canyon was La Jolla Canyon (California). The results by *Shepard* [1974] and *Gordon and Marshall* [1976] showed that steep canyons can act as a trap for tidally generated internal waves. Specifically, it was recognised that the dynamical processes occurring in canyons strongly depend on the ratio of the maximum bottom steepness ($S_{topo} = \partial H/\partial l$) (here $H(x, y)$ is the water depth, and l is the direction of the seabed depth gradient vector) to the inclination of the characteristic paths of the internal wave energy propagation

$$S_{wave} = dz/dl = \pm[(\omega^2 - f^2)/(N^2(z) - \omega^2)]^{1/2}, \quad (1)$$

where ω is the tidal frequency, f is the Coriolis parameter, and $N(z)$ is the buoyancy frequency. In other words, in terms of the mechanism of internal wave dynamics, the following parameter

$$\alpha(x, y, z) = \frac{S_{topo}}{S_{wave}} = \frac{|\partial H/\partial l|}{[(\omega^2 - f^2)/(N^2(z) - \omega^2)]^{1/2}} \quad (2)$$

is the principal measure of the bottom steepness that distinguishes two very different regimes of tidal energy conversion. Schematically they are presented in Figure 1. For specificity, the buoyancy frequency measured in a canyon of the Celtic Sea (reported in [*Vlasenko and Stashchuk*, 2015]) is used for the analysis, see Figure 1 a.

In a subcritical regime, when the condition $\alpha < 1$ is valid over the whole domain, it is mostly the lower tidal baroclinic modes that are generated. This regime is presented in Figure 1 b.

Over "steep" topographies, for which $\alpha > 1$ occurs at least for some fragments of a given slope, the supercritical regime of tidal energy conversion, presented in Figure 1 c (below point C), is fulfilled substantially increasing the conversion rate [*Gerkema et al.*, 2004]. In this regime internal tidal energy is concentrated in a narrow internal tidal beam (magenta stripe in Figure 1 c) that radiates energy away from bottom fragments where $\alpha = 1$. The energy propagates in the tidal beam upward and downward along characteristic line (1) with group velocity C_g while the wave phase propagates across the beam with the phase speed C_p, Figure 1 c. In fact, it is not only the point C with $\alpha = 1$ that is the area of the beam formation. A wider area A-B where the bottom inclination is close to critical is the place of the beam generation. More on different regimes of tidal energy conversion can be found in [*Vlasenko et al.*, 2005].

Note that intensity of the tidal beam depends not only on the relative steepness of the bottom or strength of the tidal current. It is also controlled by smoothness of the buoyancy frequency profile. In highly intermittent media with sharp vertical changes of the buoyancy frequency the downward propagated tidal energy is reflected back from the layered structures in the form of secondary tidal beams propagating to the free surface [Grimshaw et al., 2010]. This process can even lead to a complete attenuation of the tidal beam [*Gerkema and van Haren*, 2012]. However, as it was shown by *Vlasenko and Stashchuk* [2015], the surface 1.5 km layer of the Celtic Sea (which is in the focus of the present study) is mostly unaffected by internal reflection.

Note that the tidal beam is a superposition of many baroclinic modes, as it was clearly shown in the analytical solution for internal tides at abrupt topographies by *St. Laurent et al.* [2003], and the presence of a beam is evidence of higher mode excitation. For a typical "V"-shaped canyon with $\alpha \geq 1$, the baroclinic tidal energy is trapped inside the canyon, being able only to propagate downward reflecting many times from canyon's steep flanks without any opportunity of escape (see, for instance, Figure 2 in [*Balmforth and Peacock*, 2009]).

The importance of the relative bottom steepness α for internal wave dynamics in canyons was acknowledged by *Petruncio et al.* [1998] in their interpretation of measurements conducted in another well-studied canyon, Monterrey Submarine Canyon. In further analysis by *Zhao et al.* [2012], who investigated the energetic characteristics of internal waves and turbulent mixing in the canyon, it was suggested that the topographic steepness does control the energy conversion rate.

Some studies on the baroclinic dynamics in canyons were conducted for an idealized bottom profiles by *Baines* [1983]; *St. Laurent et al.* [2003]; *Grimshaw et al.* [1985]; *Zhang et al.* [2014]. A more realistic model set up, specifically, the real bottom topography, was taken in a further series of numerical experiments performed for Monterey Submarine Canyon area: *Petruncio et al.* [2002] used POM, *Jachec et al.* [2006] operated with SUNTANS, and *Hall and Carter* [2011] used POM to investigate internal tides in the canyon area. However, the specific role of the relative steepness α of the canyon topography in the distribution of the baroclinic wave energy was not investigated in any of these studies. Specifically, the structure of the baroclinic tidal field in the areas where $\alpha > 1$, a common occurrence, has not hitherto been discussed in detail.

The purpose of this paper is to interpret the three-dimensional effects of internal tidal dynamics that are seen to occur in supercritical canyons. In particular, an original observational data set collected in a supercritical canyon in the Celtic Sea is analysed here in terms of the focusing of internal tidal energy radiated from the areas with critical bottom inclination.

2. Observations

The Celtic Sea is a 200 meter deep, wide shelf sea with a large number of headlands and canyons along its shelf edge, Figure 2 a. Observations analysed here were conducted on the 376-th cruise of the RRS "Discovery" (hereafter D376) in June 2012, as a part of the FASTNEt study to quantify the cross shelf transport on the NE Atlantic Ocean margin. With relevance to this paper, 14 repeat "yo-yo" CTD profiles were conducted at a station precisely in the middle of the Petite Sole Canyon presented in Figure 2 b. Vertical profiles were repeated with approximately one hour time interval to the depth of approximately 1000 m. In addition to the CTD probe, a downward looking TRDI WHM 300kHz LADCP was mounted on the frame, so that each CTD profile was accompanied by a vertical profile of currents.

All 14 "yo-yo" temperature profiles $T_j(z)$ ($j = 1, 2, 3, \ldots, 14$) are presented in Figure 3 a by blue lines. The red line shows an equilibrium temperature distribution calculated as an average temperature at each depth. Comparing all individual temperature profiles $T_j(z)$ with the average $T(z)$ one can see that the largest deviations of every individual profile from the average take place in two zones: in the surface 150 m layer, and between 500 m and 900 m depth. Assuming that these deviations were caused by the dynamical processes developing in the canyon, the vertical displacement ζ_j of every individual isotherm on

every profile from the averaged temperature profile can be calculated using the following formula:

$$\zeta_j = \frac{|T_j - T|}{\partial T/\partial z}$$

An average profile of isotherms displacements, calculated as $1/14\sum_{j=1}^{14}\zeta_j(z)$, is presented in Figure 3 b. It shows that the absolute maximum vertical displacements of isotherms, up to 45 m, are located in deep water, between 600 and 800 m depth. The deviation profile calculated as a maximum displacement of the isotherm from its equilibrium state is close to that shown in Figure 3 b.

Note that the maximum baroclinic horizontal velocities at the "yo-yo" station were recorded by the LADCP in the surface layer (see also [*Vlasenko et al.*, 2014]). However, Figure 3 b suggests that a comparable contribution of the 600-800 m depth layer to the internal wave energy is also expected. In order to quantify the kinetic energy of dynamical processes developing at the "yo-yo" station, an average profile of horizontal velocities for all 14 LADCP sampling was calculated as follows

$$U(z) = 1/14\sum_{j=1}^{14}\sqrt{u_j^2(z) + v_j^2(z)}.$$

Here $u_j(z)$ and $v_j(z)$ $(j = 1, 2, \ldots, 14)$ are eastward and northward velocities.

The mean profile of $U(z)$ is presented in Figure 3 c (magenta line). It shows the speed maximum at the free surface as well as a secondary local maxima at the depth of 680 m which coincides with the position the maximum vertical displacement and a broad region of elevated currents between 600 m and 800 m, produced presumably by the action of internal waves.

As a proxy-measure for the relative strength of diapycnal mixing, we follow the method of *Polzin et al.* [2002] in computing the buoyancy-normalised LADCP shear in overlapping segments (50% overlap), each of 128 meters in vertical extent. The spectra for each segment were then integrated between vertical wavelengths of 25 m to 128 m, to give 14 profiles of shear variance, a property that scales with the diapycnal eddy diffusivity. The time averaged vertical profile of the shear variance (Figure 3 d) demonstrates a relative 7-fold increase below 700 m depth, with a broad maximum at 780 m. The necessary segmentation of the data results in loss of vertical resolution in comparison with temperature or velocity profiles, but nevertheless a consistent deep maximum in fine-structure derived vertical mixing is clearly apparent.

Intensification of vertical and horizontal motions in the layer between 500 and 800 m depth, classified above as a consequence of internal waves action is confirmed by Figure 4, where the temperature and eastward horizontal velocity profiles recorded at all 14 CTD stations are shown as time series. Both panels reveal semidiurnal periodicity of the recorded signals, with strong baroclinic contributions (note the intensification of horizontal currents and vertical oscillation in the surface 200 m, which is consistent with Figure 3). The most interesting feature of Figure 4 a is clear evidence of intensive semidiurnal periodicity below 500 m depth (white dashed line in panel a) with relatively quite background between 500 and 200 m.

Horizontal currents also reveal semidiurnal periodicity, most clearly seen in the surface 400 m layer. At first glance this periodicity can be attributed to barotropic tidal motions. However, weakening of the tidal signal below 400 m, and its vertical intermittency in the deep layers suggests that there should also be a strong contribution of a baroclinic signal.

Moreover, analysing the relative location of minima and maxima of the velocity pattern in space and time one can conclude that Figure 4 b can be treated as evidence of evolution of a baroclinic tidal beam with its phase moving upward (as it is presented in Figure 1 c). Co-phase segments of the beam are marked in Figure 4 b by white dashed lines. It is interesting to note that similar features have been found also in the model output which was applied in this paper to replicate the tidal dynamics in the canyon area. The results of modelling are discussed in the next section.

In order to bring more clarity to the interpretation of these relatively sparse observations and to understand the reasons for apparent internal wave energy and vertical mixing intensification in the deep part of the canyon, a series of numerical experiments was conducted.

3. Model results

The fully non-linear non-hydrostatic MITgcm was used to model internal tides in the canyon and the surrounding area (see Figure 2 b). In the main part of the model domain the horizontal and vertical resolutions were 100 m and 10 m, respectively. In order to avoid any spurious boundary reflections, an exponentially increasing horizontal grid step near the lateral boundaries was used that guaranteed an accurate numerical solution within the internal model domain without any signals reflected from the boundaries during at least 10 tidal cycles.

The tidal forcing was set in the model by a tidal potential added to the right hand side of the momentum balance equations. Its intensity was chosen using TPXO8.0 [*Egbert and Erofeeva*, 2002] in such a way as to reproduce tidal velocities recorded by moored ADCP current meters deployed during D376 that have shown the predominance of semi-diurnal

M2 tidal harmonic [*Vlasenko et al.*, 2014]. Spatial distribution of tidal ellipses is shown in Figure 2 d. A vertical stratification was introduced into the model after setting the tidal forcing for a homogeneous fluid. The temperature and salinity profiles were taken from the direct CTD measurements at the yo-yo station.

The Richardson number dependent parametrization for vertical viscosity ν and diffusivity κ introduced in [*Pacanowski and Philander*, 1981] was used:

$$\nu = \frac{\nu_0}{(1+\beta \mathrm{Ri})^n} + \nu_b, \quad \kappa = \frac{\nu}{(1+\beta \mathrm{Ri})} + \kappa_b.$$

Here Ri is the Richardson number, $\mathrm{Ri} = N^2(z)/(u_z^2 + v_z^2)$, u and v are the components of horizontal velocity; $N(z)$ is the buoyancy frequency $N^2(z) = -g/\rho(\partial\rho/\partial z)$ in which g is the acceleration due to gravity and ρ is the water density; ν_b=10^{-5} m^2 s^{-1} and κ_b=10^{-5} m^2 s^{-1} are the background viscosity, and diffusivity, respectively; ν_0=$1.5{\cdot}10^{-2}$ m^2 s^{-1}, β=5 and n=1 are the adjustable parameters. Such a parametrisation increases ν and κ in areas where the Richardson number is small. The horizontal viscosity and diffusivity were set to a constant value of 0.5 m^2 s^{-1}. More details on the model initialization and input parameters can be found in *Vlasenko et al.* [2014].

The principal question to be addressed by the modelling efforts is to identify the cause of the highly energetic internal wave activity in the centre of the canyon below 500 m depth. The modelling evidence of this intensification in deep water is seen in Figure 5 where the amplitude of the model-predicted horizontal velocities

$$U_{\max}(x,y,z) = \sqrt{u^2_{\max}(x,y,z) + v^2_{\max}(x,y,z)}.$$

is presented. Here $u_{\max}(x,y,z)$ and $v_{\max}(x,y,z)$ are amplitudes of the eastward and northward velocities found over one tidal cycle at the position (x,y,z).

Nine horizontal slices of the velocity $U_{\max}$ at depths of between 300 m and 700 m presented in Figure 5 reveal quite a curious tendency. In the surface layers, i.e. shallower than 500 m, the wave energy is mostly concentrated at the periphery of the canyon corresponding to the shelf break area. However, below this depth the regions with high energy concentration are mostly located within the centre of the canyon, not around its edge. This finding is consistent with the observational profiles shown in Figures 3 b and c that reveal the energy maximum at approximately 700 m depth recorded at the CTD station in the middle of the canyon.

Such a focusing of internal wave energy in the canyon's centre can be explained in terms of a superposition of several tidal beams generated at the shelf edge on the periphery of the canyon and radiating downward toward the centre of the canyon, as it is shown in Figure 1 c. Indeed, analysis of the bottom steepness (2) has shown that $\alpha << 1$ in the surrounding shelf area, but $\alpha > 1$ in the central part of the canyon, see Figure 6 a. The red zones here, situated along the shelf break, separate the areas of subcritical shelf from the supercritical abyssal part of the canyon.

It is important to note that the positions of the potential generation cites of tidal beams (as sectors A-C shown in Figure 1 c) correlate very well with the locations of the internal body force (IBF) introduced by *Baines* [1982] for quantification of the the tidal energy conversion. In a two-dimensional (x, z) case the IBF reads:

$$F = \rho Q z \frac{N(z)^2}{\omega} \left(\frac{1}{H(x)} \right)_x .$$

Here Q is water discharge produced by tides and ρ is the reference density. Being integrated from the surface to the bottom this formula gives an overall efficiency of the internal tide generation for the whole water column, $\Phi = \int_{-H}^{0} F dz$. In a three-dimensional case

(x, y, z) the vertically integrated IBF in every point is calculated using the discharge and the derivative $\partial(1/H)/\partial l$, where l in the direction of the depth gradient, as shown in formulae (2). The spatial distribution of the vertically integrated IBF Φ shown in Figure 6 b was calculated for the stratification presented in Figure 1 a and the tidal forcing depicted in Figures 2.

Figure 6 a demonstrates that the main part of the canyon topography is supercritical for semi-diurnal internal tidal waves with the maximum IBF concentrated around the canyon rim. As a result, according to theory [*Vlasenko et al.*, 2005], the internal tide in the canyon should take a form of tidal beams generated at the shelf break around the canyon periphery which radiate downward toward the centre of the canyon, as is shown in the scheme depicted in Figure 7. Bearing in mind that the canyon head has a near-circular shape, it is expected that it can function like an optical lens focusing wave energy into its centre. Evidence for that interpretation is presented in Figure 8 a for the vertical cross-section depicted in Figure 2 b by a white line. Three tidal beams can be identified in Figure 8 a (the characteristic lines, equation (1), are shown here by thin white lines). The tidal beam *a*-*b*-*c* is generated at the shelf break point, at *b*, and propagates downward along characteristic line *b*-*c*. The internal wave beam pattern, resembling a St.Andrews cross, is generated at the saddle point *e*. The tidal energy propagates from this point along four characteristic lines, *e*-*g*, *e*-*d*, *e*-*h*, and *e*-*f*. It is interesting and relevant to note that the two tidal beams generated at the opposite sides of the canyon, viz. *b*-*c* and *e*-*f* meet in the centre of the canyon in the layer between 600 and 800 m depths which is consistent with the position of the deep-water maxima in vertical displacement, horizontal velocity and shear variance seen in Figures 3 d.

Observational evidence of the tidal beam can also be found in Figures 4 b where the northward horizontal velocity recorded at the yo-yo station is presented as a time series. It correlates well with Figures 9 d where similar signal, predicted by the MITgcm at the position of the yo-yo station, is presented. Consistency of both patterns is obvious, although the observational one is less contrasted and more noisy. Both panels reveal upward propagation of the wave phase (shown by dashed white lines in Figures 4 b and 9 b), which can be treated in terms of the tidal beam evolution schematically presented in Figures 1 c.

Model predicted vertical displacements of the isotherms below 400 m depth are a bit larger than those recorded in-situ (compare Figures 4 a and 9 a), although both panels demonstrate evidence of semidiurnal periodicity (find white dashed lines) and relatively "calm" internal wave activity in the intermediate layers (between 150 and 350 m).

As seen from Figure 6, similar conditions of the energy focusing discussed above, i.e. position of sub-, and supercritical areas, are valid also for many other cross-sections passing through the centre of the canyon. In other words, the tidal energy is converted at many particular areas around the canyon periphery, and is then radiated towards its centre and accumulated there at the depths of between 500 and 800 m, as is observed in the CTD/LADCP analysis.

Such focusing of wave energy in the canyon's centre should increase the associated level of local water mixing there, since energy cannot accumulate indefinitely. Elevated shear variance is testament to greater elevated mixing at depth (Figure 3 d). Model results demonstrate a similar increase of vertical diapycnal mixing. Figure 10 shows that the coefficient of vertical diffusivity κ in the centre of the canyon calculated using

the Richardson number dependent parametrization [*Pacanowski and Philander*, 1981] increases from the background level κ_b=10^{-5} m^2 above 500 m depth up to 10^{-2} m^2 in the layer from 600 m to 800 m depth where the tidal beam meet in the centre of the canyon. This dramatical increase suggests strong diapicnal mixing in the place of tidal beam focusing. As a result of intensified local diapycnal mixing, a quasi stationary density (temperature) gradient is formed across the canyon, as shown in Figure 8 b (the same cross-section as in Figure 8 a). Convergence and divergence of isotherms at the depths of between 500 m to 900 m is clearly seen here from two pairs of isotherms colored in white and magenta. Initially (before the model run) the distance between both (parallel) isolines was equal to 100 m: the upper and lower "white" isotherms were initially at depths of 650 m and 750 m, respectively; the upper and lower "magenta" isotherms were initially at depths of 800 m and 900 m. After ten cycles of tidal action the distance between the two groups of isotherms was modified: at some positions they converged, and at others they diverged. Figure 11 shows the difference between isotherms initially centred at 700 m (Figure 11 a) and at 850 m (Figure 11 b). It is interesting that the convergence and divergence of isolines is opposite for the two depth pairs, Figure 11 a, b.

The formation by diapycnal mixing of quasi-stationary horizontal pressure gradients suggests the existence of geostrophically balanced baroclinic eddies. A quasi-stationary eddy is clearly seen in Figure 12 in the velocity vector fields at depths of 450 m, 600 m and 700 m. It was obtained by subtraction of the barotropic tidal flow (at each point it was found as an average value of the velocity through the whole water column from surface to the bottom) and by averaging of all fields over several tidal periods in order to exclude periodic tidal motions and to reduce noise. The eddy around the topography bank is

seen at a depth of 450 m where the tidal beam is still located close to the canyon flank and the shelf edge. However, vortical motions are absent in the centre of the canyon at this depth (450 m). According to the findings presented above, the tidal energy is mostly concentrated beneath 450 m and in the centre of the canyon. Here a baroclinic eddy with anti-cyclonic rotation at 600 m depth and cyclonic rotation at 700 m depth is clearly seen.

Note that the correct choice of the model parameters for the turbulent closure that produces an adequate eddy pattern is not always possible without validation of the model output against observational data. In our case we used observations by *Inall et al.* [2000] conducted over the Malin Sea continental slope adjacent to the considered here area. Direct in-situ measurements of the background turbulence allowed them to quantify the vertically integrated coefficient of turbulent diffusion in the range (5-12)$\cdot 10^{-4}$ ($m^2 s^{-1}$). Integration of the vertical profile of diffusivity shown in Figures 10 produced by the model returns the value of $7.5 \cdot 10^{-4}$ ($m^2 s^{-1}$) (shown by a dashed line) which is well inside of the in-situ observed range.

To find observational evidence of the predicted baroclinic eddy generated in the middle of the canyon, the following analysis of the LADCP data was performed. First, the barotropic velocities U_j^{bar} and V_j^{bar} were found by averaging of the instant velocity profiles:

$$U_j^{\mathrm{bar}} = \frac{1}{H_j} \int_0^{H_j} u_j(z) dz;$$

$$V_j^{\mathrm{bar}} = \frac{1}{H_j} \int_0^{H_j} v_j(z) dz.$$

$j = 1, 2, 3, \cdots, 14$. Second, the barotropical tidal signal was removed from the sampling data using the following procedure:

$$u_j^{\rm int} = u_j - U_j^{\rm bar};$$

$$v_j^{\rm int} = v_j - V_j^{\rm bar},$$

It is clear that the remaining baroclinic signals $u_j^{\rm int}$ and $v_j^{\rm int}$ contain both mean currents and internal waves. They are also not free from a random signal that always is present in any observational data set. In order to reduce the noise average vertical profiles of both components were calculated as follows: $u^{\rm int}(z) = 1/14\sum_{j=1}^{14} u_j^{\rm int}(z)$ and $v^{\rm int}(z) = 1/14\sum_{j=1}^{14} v_j^{\rm int}(z)$. In addition, vertical averaging of $u^{\rm int}(z)$ and $v^{\rm int}(z)$ in 100 m thick layers with centres at depths 600 m and 750 m was conducted. The resulting vectors along with the model predicted vectors are presented in Figures 13 a and 13 b. Looking at the averaged velocity vectors one can discern a good consistency. It seems that the direction of the black arrows in Figures 13 a and 13 b is consistent with that predicted by the model, i.e. the anti-cyclonic and cyclonic rotation in depths 600 m and 750 m layers, respectively. This can be considered as further evidence that tidal energy focusing in the centre of the canyon is responsible for the formation of baroclinic eddies there.

4. Two-dimensional versus three-dimensional focusing

The importance of three-dimensional effects in focusing of baroclinic tidal energy in the centre of a circular canyon (as shown in Figure 7) can be demonstrated and quantified more accurately by comparing three-dimensional (3D) and two-dimensional (2D) simplified cases. In doing so a series of numerical experiments was conducted for two idealized canyons, shown in Figures 14. The shape of both canyons in the x-direction was the same,

i.e. $H(x) = H_0 + H_m \cos^2(\pi x/2l)$, although in a 2D case the canyon was indefinitely long in the y-direction to exclude influence of the y-derivatives, but its 3D counterpart has circular form, see Figures 14 b. The parameters of the bottom topography were taken realistic, i.e. H_0 =200 m, H_m =800 m, l =7.5 km. The buoyancy frequency in this series of experiments was taken according to profile shown in Figures 1 a, but the intensity of the tidal forcing was taken ten times weaker than in Section 3 in order to reduce the influence of non-linear terms and to show the effect of tidal energy focusing more clearly.

Two systems of tidal beams are generated at either sides of both canyons. In Figure 14 they are presented as a series of instant horizontal velocity fields both for 2D (upper panels) and 3D (bottom panels) canyons. Tidal energy is radiated upward and downward from the shelf edges propagating in narrow bands along characteristic lines (1). Downward propagating tidal beams meet in the centre of the canyons at the depth of about 550m and amplify each other creating a spots of high tidal activity. Propagating further downward the tidal beams experience multiple reflections from the canyon flanks and produce amplification of tidal energy in the canyon centres. As a result of narrowing cross-section of canyons down to the deep the intensity of tidal motion increases. This effect is clearly seen in all six panels presented in Figure 15.

The comparison analysis of the top and bottom panels shows that the structure of the wave fields in two- and three-dimensional canyons is a bit different. Note also quite a different level of intensity of baroclinic motions in both canyons. They look weaker near the surface in the 3D case, but stronger in its deep part.

In order to quantify the difference more accurately the amplitude of the baroclinic tidal energy $E = 0.5\rho(u^2+v^2+w^2+N^2\xi^2)$ was calculated (here u, v, and w are the components

of the velocity vector, N is the buoyancy frequency, ξ is isopicnal displacement, and ρ is the water density). The amplitude values of energy density are presented in Figure 16 both for 2D and 3D canyons. Four control points with maximum of local tidal energy have been chosen for the comparative analysis: the point **a** near the shelf break where tidal beams are generated, points **b** and **c** in the deep part where the beams intersect, and point **d** with the highest level of concentration of baroclinic tidal energy (near the bottom). The appropriate values of the energy density were 24, 31, 32 and 43 Jm^{-3} for the 2D canyon, and 16, 36, 61 and 50 Jm^{-3} for the 3D one. From this series of experiments it is clear that a 2D canyon is more efficient in terms of the tidal energy conversion demonstrating 1.5 larger value of baroclinic tidal energy at the shelf break. At the same time the intensity of the baroclinic tidal motions in the deep is much higher in the three-dimensional case. In fact, the 3D canyon works as an optical lens focusing the tidal energy from all directions into a focal centre. Even though the tidal beams generated at the shelf break of the 3D canyon are 1.5 times weaker than in a 2D case, the 3D focusing provides two times larger density of baroclinic tidal energy in the deep part of the canyon than its 2D counterpart.

The increase of baroclinic tidal energy in the deep part of the 3D canyon compared to that in surface layers results in larger level of diapicanal mixing and formation of stronger geostrophically adjusted eddies near the bottom. This fact is clearly seen in Figure 17 where vectors of the velocity fields averaged over one tidal cycle at depths 800 m, and 900 m are presented. These two sections coincide with the positions of the maximum of tidal energy concentration depicted in Figure 16 b by letters **c** and **d**. Both patterns demonstrate evidence of an anticyclonic eddy with the velocities at the level of 1 cms^{-1}. Note, however, that the currents near the bottom at the depth of 900 m on average are

two time stronger than that at 800 m depth. This is consistent with Figure 16 b which demonstrates higher energy concentration near the bottom.

5. Discussion and conclusions

Submarine canyons are common bathymetric features at many of the world's shelf edge regions. They can trap internal wave energy holding it towards the head of canyons in a converging wave-guide that can lead to a high level of turbulent mixing there. This mechanism was discussed by *Baines* [1983]; *Gardner* [1989]; *Gordon and Marshall* [1976]; *Hotchkiss and Wunsch* [1982]. Note, however, that the aforementioned papers appeal predominantly to a two-dimensional concept of this mechanism. In reality one should operate with three-dimensional characteristic surfaces of a 3D wave equation rather than with the characteristic lines of its 2D counterpart. As a result of the three-dimensionality, the tidal beams emanating from flanks of a concave topography can focus in its centre producing a spot with high levels of internal wave energy and mixing. This paper deals with the three-dimensional aspects of this focusing mechanism.

The possibility of intensification of baroclinic tidal energy due to wave interference was recently reported in a number of theoretical papers. *Carter* [2010] analysing model output for baroclinic tide in the Monterrey Bay region testified interference of internal waves generated at different sectors of the bay. It was found that the model predicted up to 5 times increase of the baroclinic tidal flux close to the Monterrey canyon axis located in the centre of the bay. It was hypothesized there that the effect was created thanks to topographic focusing, although this fact was not clarified, specifically in terms of the beam-like structure of baroclinic tides or supercriticality of the bottom topography.

Similar effects of the interference of baroclinic tidal energy radiated from scattered multiple sources were also reported by *Rainville et al.* [2010] for the Hawaiian Ridge area. As distinct from the present study, mostly horizontal interference of the baroclinic tidal waves was studied, however the effect of baroclinic tidal energy superposition was clearly demonstrated.

The most recent model study conducted by *Zhang et al.* [2014] for an idealized and supercritical for semi-diurnal M2 tide canyon confirmed an asymmetry of internal tide near the canyon, which presumably is a consequence of the along-shore effects of propagating internal tidal wave. In fact, they focus mostly on resonant effects of internal tide generation in the canyon and its beam-like onshore propagation alongside explanation of the reasons for the asymmetry of tidal fields. With relevance to the present study, *Zhang et al.* [2014] reported the beam-like structure of baroclinic tides near the supercritical canyon, with a difference in deepward and shoreward structures, although their interference in the canyon area was not demonstrated.

Model output always allows us to study the process of wave focusing in detail, however in reality it is quite difficult to observe this effect in-situ. For the Celtic Sea we have found not only theoretical but also observational evidence of the baroclinic tidal energy focusing in the middle of the canyon. The measurements were conducted during D376 in the centre of the Petite Sole Canyon situated at the shelf edge of the Celtic sea (see Figures 2). CTD and LADCP data collected at a station in the middle of the canyon revealed large vertical oscillations of isotherms (up to 45 m, Figures 2 b) and local maximum of horizontal currents (up to $0.12\,\mathrm{ms}^{-1}$, Figures 3 c) in the layer between 500 and 800 m.

The possibility of such an inherently three dimensional focusing mechanism of baroclinic tidal energy was confirmed in a series of numerical experiments conducted using the MITgcm forced by M2 tidal harmonic. The high internal tidal activity in the deep part of the canyon (Figures 5) is treated here in terms of downward propagation and focusing of internal tidal beam generated at the shelf break. The specific circular shape of the canyon, coupled with the steep bottom topography below the shelf break (steeper than tidal beam) in all parts of the canyon create favourable conditions for the tidal energy focusing in the canyon's centre, see Figure 7. Both observations and MITgcm simulations have also shown that the tidal energy focusing intensifies local diapycnal mixing (Figures 3 d and 10), that can lead to formation of a baroclinic eddy below 450 m depth in the central part of the canyon, see Figures 12. Evidence consistent with the presence of the cyclonic and anti-cyclonic rotation in the canyon centre was found also in in-situ data.

The importance of the results is that the effect of the focussing of baroclinic tidal energy in 3D configuration is quite a typical situation in many areas. This means that the results on the baroclinic tidal energy focusing reported here can have much wider application rather than just circular-shape canyons.

Acknowledgments. This work was supported by the Natural Environment Research Council Grant FASTNEt (award NE/I030259/1). The used data are available at http://www.sams.ac.uk/fastnet.

References

Baines, P.G. (1982,) On internal tide generation models, *Deep Sea Res. I*, *29*, 307–339.

Baines, P.G. (1983), Tidal motion in submarine canyons a laboratory experiment, *J. Phys. Oceanogr.*, *13*, 310–328.

Balmforth, N.J. and T. Peacock (1983), Tidal conversion by supercritical topography, *J. Phys. Oceanogr.*, *13*, 310–328.

Carter, G.S. (2010), Barotropic and baroclinic M_2 tides in Monterey Bay region, *J. Phys. Oceanogr.*, *39*, 1965–1974.

Egbert, G.D., and S.Y. Erofeeva (2002) Efficient inverse modeling of barotropic ocean tides, *J. Atmos. Oceanic Technol., 19(2)*, 183–204.

Gardner, W.D. (1989), Periodic resuspension in Baltimore Canyon by focusing of internal waves, *J. Geophys. Res.*, *94(C12)*, 18,185–18,194.

Gerkema, T., F.A. Lam, and L.R. Maas (2004), Internal tides in the Bay of Biscay: conversion rates and seasonal effects *Deep-Sea Res. II*, *51*, 2995–3008.

Gerkema, T., and H. van Haren (2012), Absence of internal tidal beams due to non-uniform stratification. *J. of Sea Res.*, *74*, 2–7.

Gordon, R.L., and N.F. Marshall (1976), Submarine canyons: internal wave traps? *Geoph. Res. Let.*, *3(10)*, 622–624.

Grimshaw, R.H.J., P.G. Baines, and R.C. Bell (1985), The reflection and difraction of internal waves from the junction of a slit and a half-space, with application to submarine canyons. *Dyn. Atmos. and Oceans*, *9*, 85–120.

Grimshaw R., E. Pelinovsky, and T. Talipova (2010), Non-reflecting internal wave beam propagation in the deep ocean *J. of Phys Oceanogr.*, *40*, 802-813.

Hall, R.A., and G.S. Carter (2011), Internal tides in Monterrey Submarine Canyon, *J. Phys. Oceanogr.*, *41*, 186–204.

461 Hickey, B.M. (1995), Coastal submarine canyons, *Topographic Effects in the Ocean: 'Aha*
462 *Huliko'a Hawaiian Winter Workshop*, Honolulu,HI, University of Hawaii at Manoa,
463 95–110.

464 Hotchkiss, F.S., and C. Wunsch (1982), Internal waves in Hudson Canyon with possible
465 geological implications, *Deep-Sea Res.*, *29(4A)*, 415–442.

466 Inall, M.E., T.P. Rippeth, and T.J.Sherwin (2000), Impact of nonlinear waves on the
467 dissipation of internal tidal energy at a shelf break, *J. Geophys. Res.*, *115(4)*, 8687–
468 8705, doi:10.1002/2013JC009708.

469 Jachec, S.M., O.B. Fringer, M.G. Gerritsen, and R.L. Street (2006), Numerical simulation
470 of internal tides and the resulting energetics within Monterrey Bay and the surrounding
471 area, *Geoph. Res. Let.*, *33*, doi:10.1029/2006GL026314.

472 Kunze, E., L.K. Rosenfeld, G.S. Carter, and M.C.Gregg (2002), Internal waves in Mon-
473 terrey Submarine Canyon, *J. Phys. Oceanogr.*, *32*, 1890–1913.

474 Pacanowski, R.C., and S.G.H. Philander (1981) Parameterisation of vertical mixing in
475 numerical models of Tropical Oceans, *J. Phys. Oceanogr.*, *11*, 1443-1451.

476 Petruncio, E.T., L.K. Rosenfeld, and J.D. Paduan (1998), Observations of the internal
477 tide in Monterrey Canyon, *J. Phys. Oceanogr.*, *28*, 1873–1903.

478 Petruncio, E.T., J.D. Paduan and L.K. Rosenfeld (2002), Numerical simulation of the
479 internal tide in a submarine canyon, *Ocean Modell.*, *4*, 221–248.

480 Polzin, K., E. Kunze, J. Hummon, and E. Firing (2002) The finescale response of lowered
481 ADCP velocity profiles, *J. Atmos. and Oceanic Technol.*, *19*, 205–224.

482 Rainville, L., T.M.S. Jonston, G.S. Carter, M.A. Merifield, R.Pincel, P.F. Worcester, and
483 B.D. Dushaw (2010), Interference pattern and propagation of the M_2 internal tide south

484 of the Hawaiian Ridge, *J. Phys. Oceanogr.*, *40*, 311–325.

485 Shepard, F. P. (1974), "Internal waves" advancing along submarine canyons, *Science*, *19*,
486 195–198.

487 St. Laurent, L., S. Srtringer, C. Garrett, and D. Perrault-Joncas (2003), The generation
488 of internal tides at abrupt topography, *Deep-Sea Res. I*, *50*, 987–1003.

489 Thurnher, A.M., L.C. St.Laurent, K.G. Speer, J.M. Toole and J.R. Ledwell (2005), Mixing
490 associated with sills in a canyon on the Midocean Ridge flank, *J. Phys. Oceanogr.*, *35*,
491 1370–1381.

492 Vlasenko V., and N. Stashchuk (2015) Internal tides near the Celtic Sea shelf
493 break: A new look at a well known problem *Deep-Sea Res.*, *103*, 24-36,
494 http://dx.doi.org:10.1016/j.dsr.2015.05.003.

495 Vlasenko V., N. Stashchuk, and K. Hutter (2005), Baroclinic tides: theoretical modeling
496 and observational evidence. Cambridge University Press. 365 pp.

497 Vlasenko V., N. Stashchuk, M.Inall, and J.Hopkins (2014), Tidal energy conversion in a
498 global hot spot: on the 3D dynamics of baroclinic tides at the Celtic Sea shelf break,
499 *J. Geophys. Res.*, *119(6)*, 3249–3265, doi:10.1002/2013JC009708.

500 Wain, D.J., M.C. Gregg, M.H. Alford, R.-C. Lien, R.A. Hall, and G.S. Carter (2013),
501 Propagation and dissipation of the internal tide in upper Monterrey Canyon, *J. Geophys.*
502 *Res.*, *18*, 4855–4877, doi:10.1002/jgrc.20368.

503 Zhang,W.Z., T.F. Duda, and I.A. Udovychenkov (2014) Modeling and analysis of internal-
504 tide generation and beamlike onshore propagation in the vicinity of shelfbreeak canyons,
505 *J. Phys. Oceanogr.*, *44*, 834–849.

506 Zhao,Z., M.H. Alford, R.C. Lien, and M. C. Gregg (2012) Internal tides and mixing in
507 submarine canyon with time-varying stratification, *J. Phys. Oceanogr.*, *42*, 2121–2142.

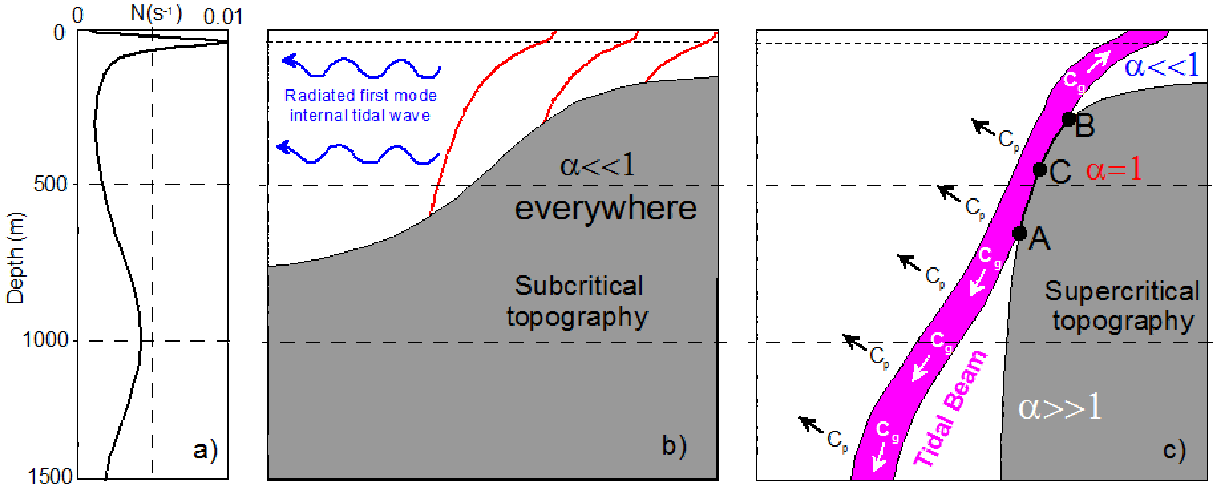

Figure 1. a) Buoyancy frequency measured in the Celtic Sea. b)-c) Schemes of the generation regime over subcritical (b) and supercritical (c) topographies. Red lines in panel (b) show characteristics (1). Magenta area in panel (c) depicts a tidal beam.

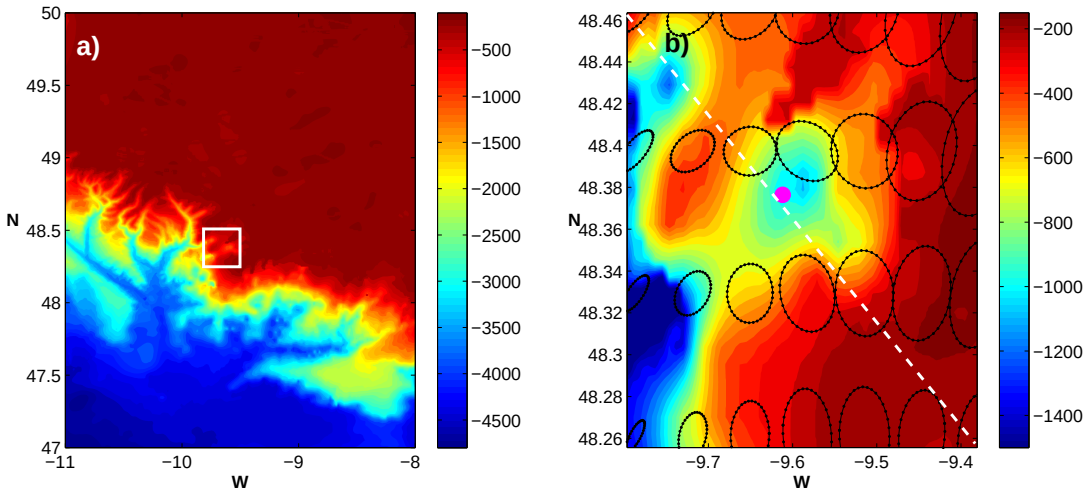

Figure 2. a) Bathymetry of the Celtic Sea. White rectangle shows the position of the canyon. b) Zoom of the Petite Sole Canyon area. The position of the yo-yo CTD station is depicted by a magenta dot. Tidal ellipses showing the intensity of the model forcing are presented by black contours.

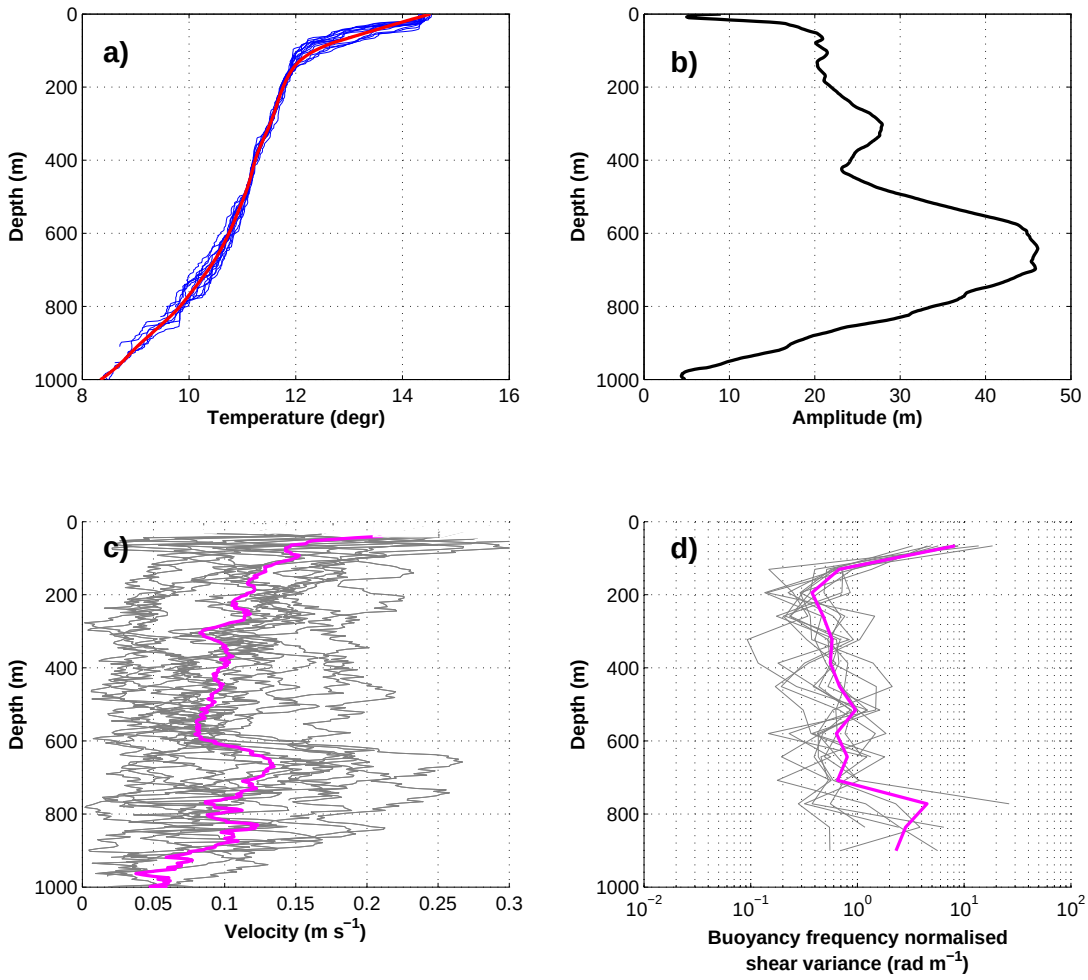

Figure 3. a) Temperature profiles recorded at 14 "yo-yo" CTD stations (blue lines) along with the average temperature profile (red line). b) Depth dependent amplitude of isotherms deviation. c) Horizontal velocity profiles recorded by LADCP (grey lines) and their mean profile (magenta line). d) Distribution of shear variance. All profiles are shown in grey and the magenta line depicts their average.

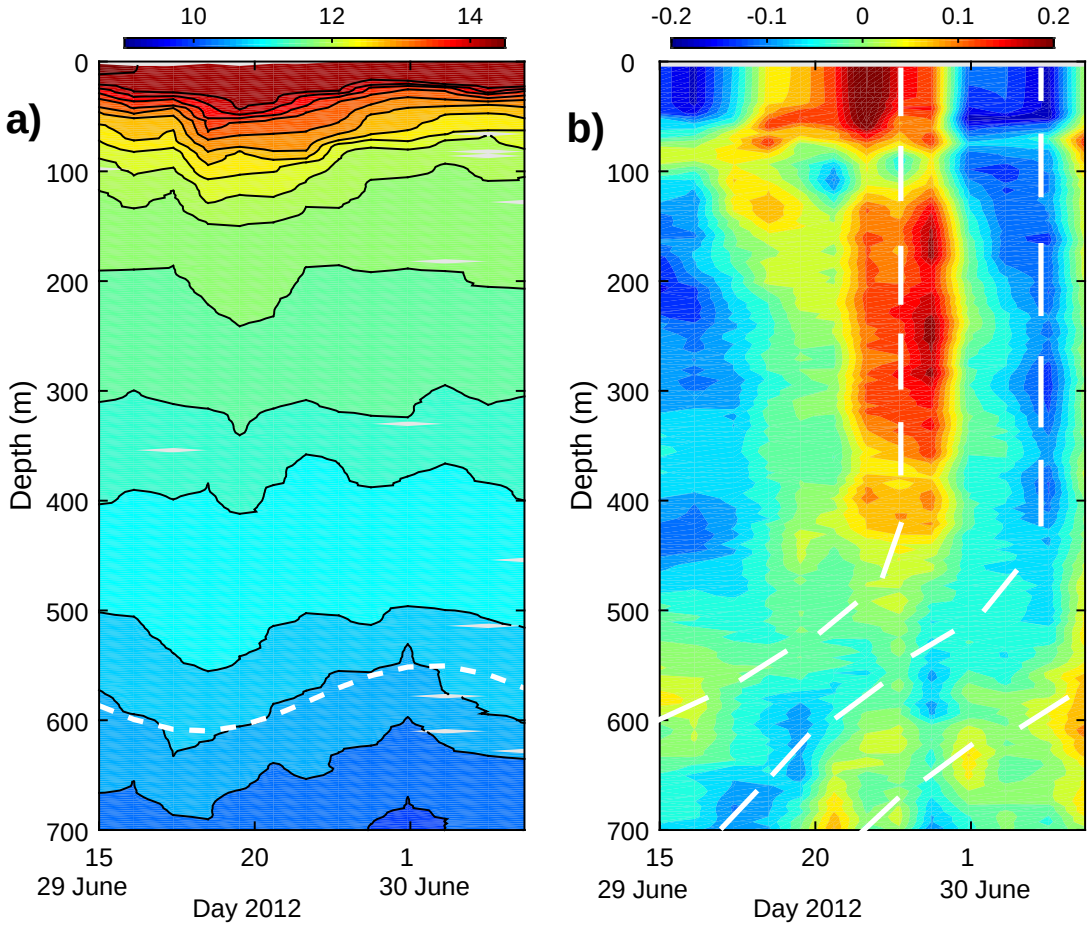

Figure 4. a) Temperature (°C) and b) eastward horizontal velocity (ms^{-1}) recorded at the "yo-yo" CTD station and presented as time series. Dashed lines in panels (b) show upward propagation of the tidal beam phase, as it is schematically shown in Figure 1 c.

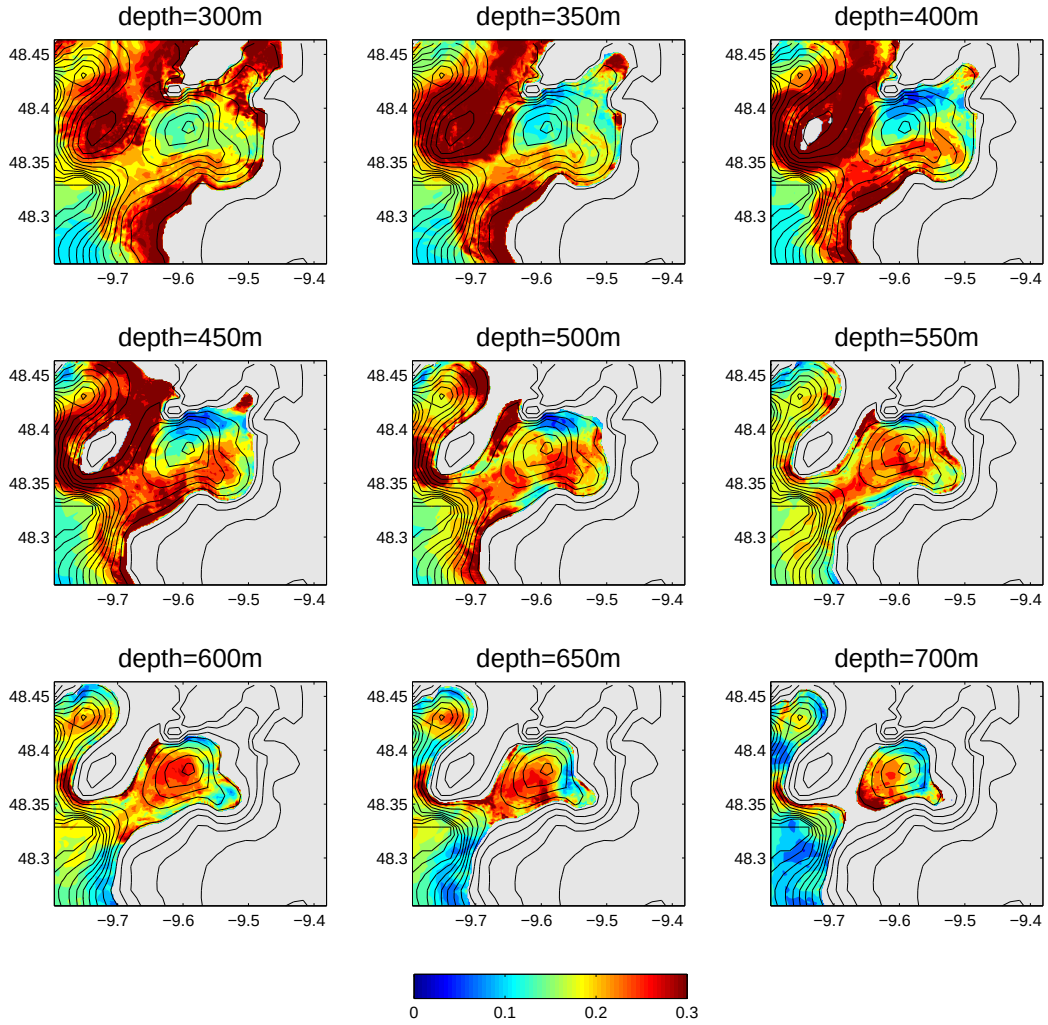

Figure 5. Horizontal distribution of the amplitudes of horizontal velocity at different depths.

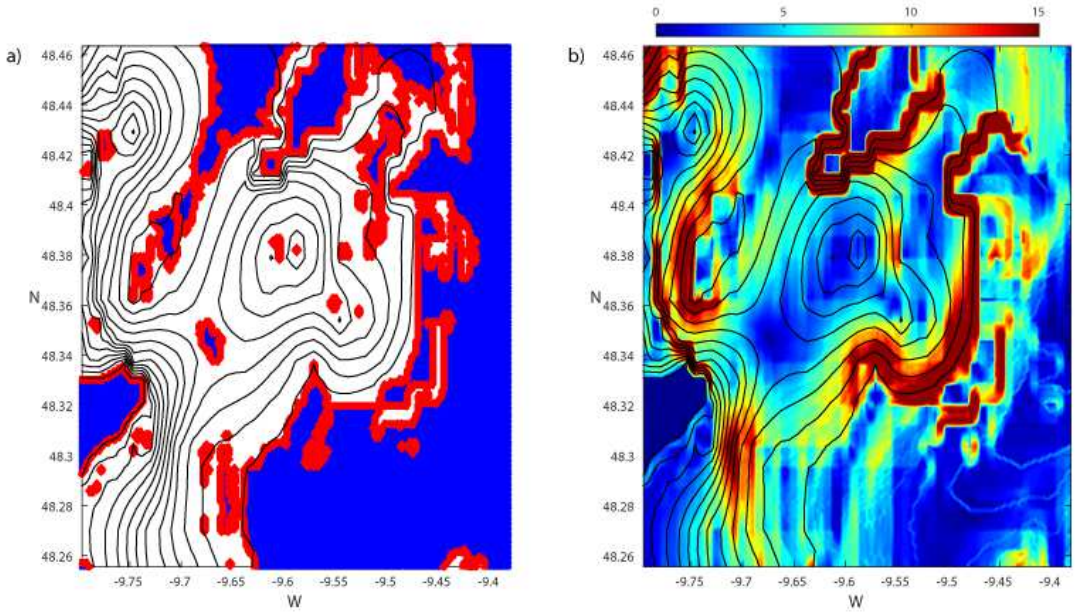

Figure 6. a) Spatial distribution of parameter α: blue areas $\alpha < 1$, red stripes $\alpha = 1$, and clear areas with $\alpha > 1$. b) Positions of vertically integrated internal body force Φ ($m^2 s^{-2}$).

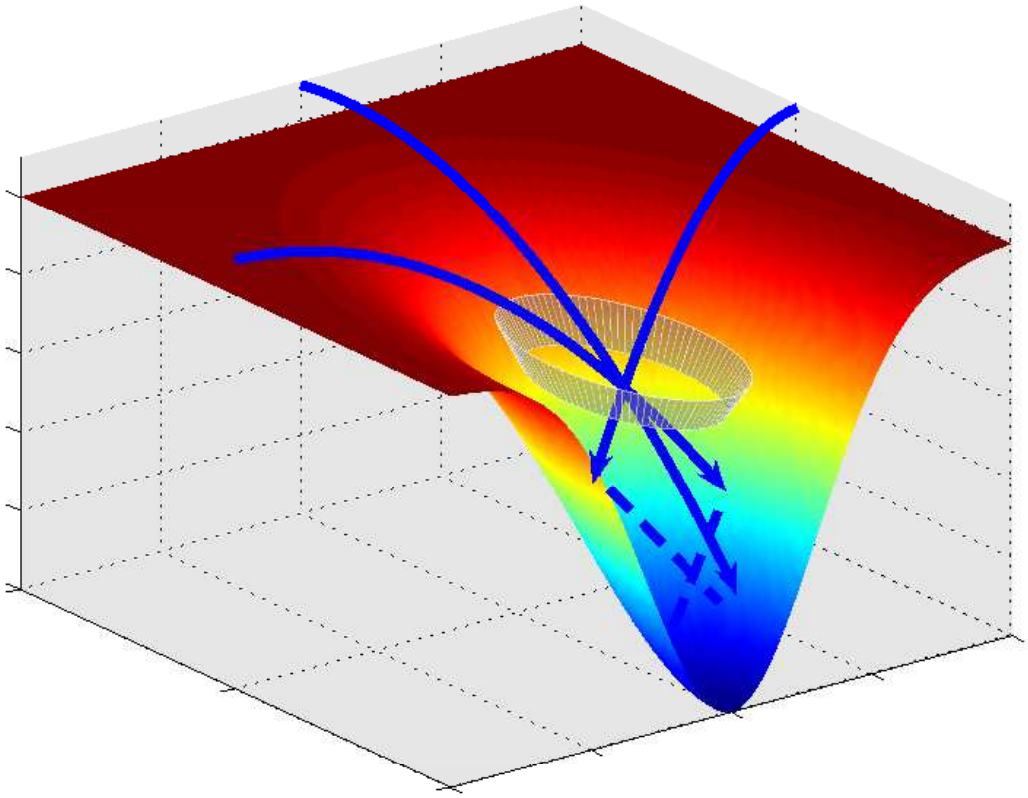

Figure 7. Scheme of interference of tidal beams in the centre of an idealized canyon with formation of a baroclinic eddy.

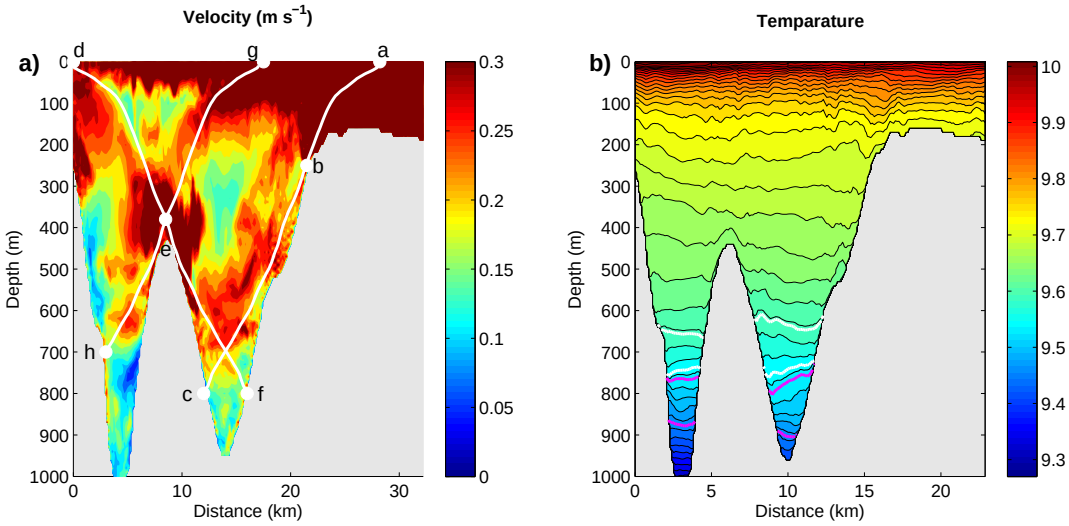

Figure 8. a) The largest values of horizontal velocity calculated for the cross-section shown in Figure 2 a. White contours depict characteristic lines (1). b) Average temperature distribution with upper white contour representing isotherm 10.55°C and the lower one 10.1°C. Similar values for two magenta isolines are 10.0°C and 9.3°C.

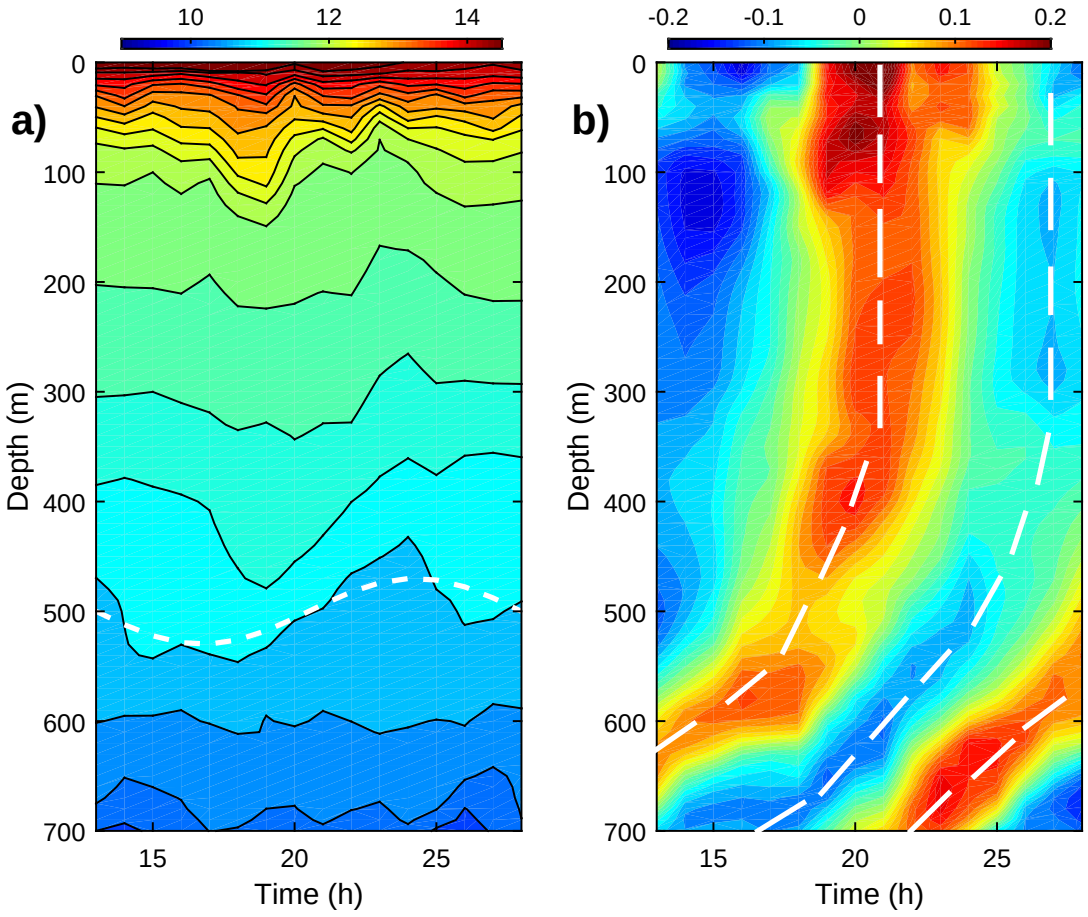

Figure 9. Model predicted a) temperature (°C) and b) eastward horizontal velocity (ms^{-1}) for the position of the "yo-yo" CTD station presented as time series. Dashed lines in the velocity panels (b) show upward propagation of the tidal beam phase, as it is schematically shown in Figure 1 c.

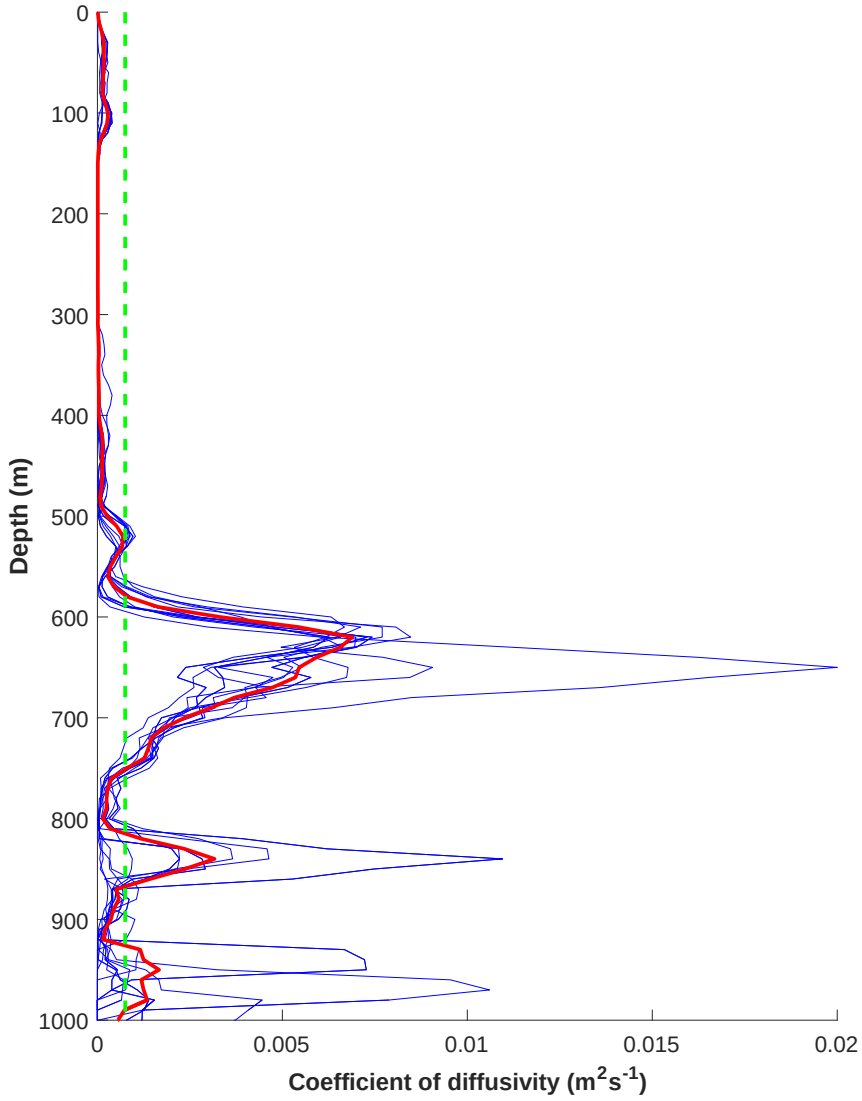

Figure 10. The coefficient of vertical diffusivity κ at the position of the yo-yo station calculated using the *Pacanowski and Philander* [1981] parametrization. Blue lines show instant profiles for the moments of yo-yo sampling, and the red line depicts an average profiles. Dashed line depicts the depth-averaged value, $7.5{\cdot}10^{-4}$ ($\mathrm{m^2 s^{-1}}$).

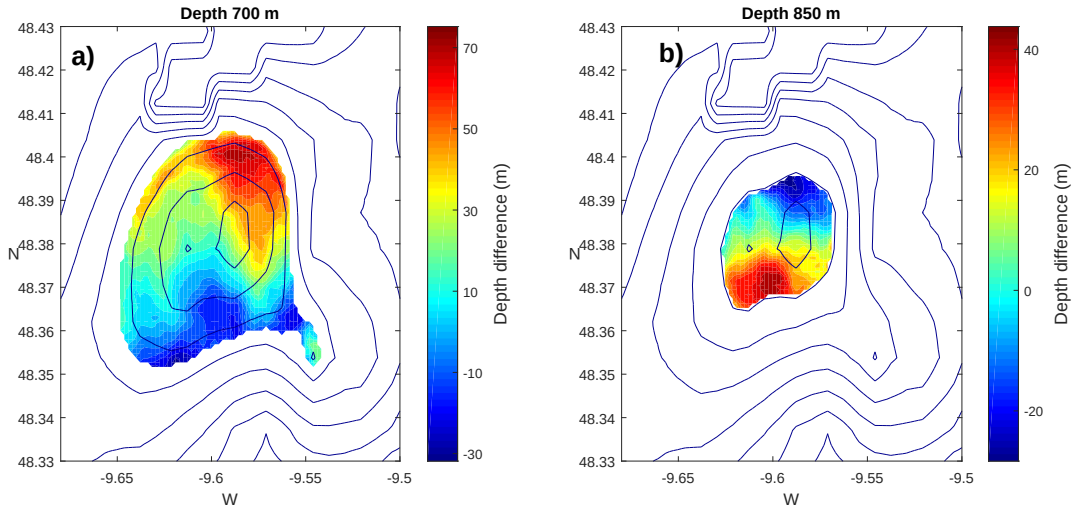

Figure 11. a) The distance between isotherms shown in Figure 8 b in white. b) The distance between isotherms shown in Figure 8 b in magenta.

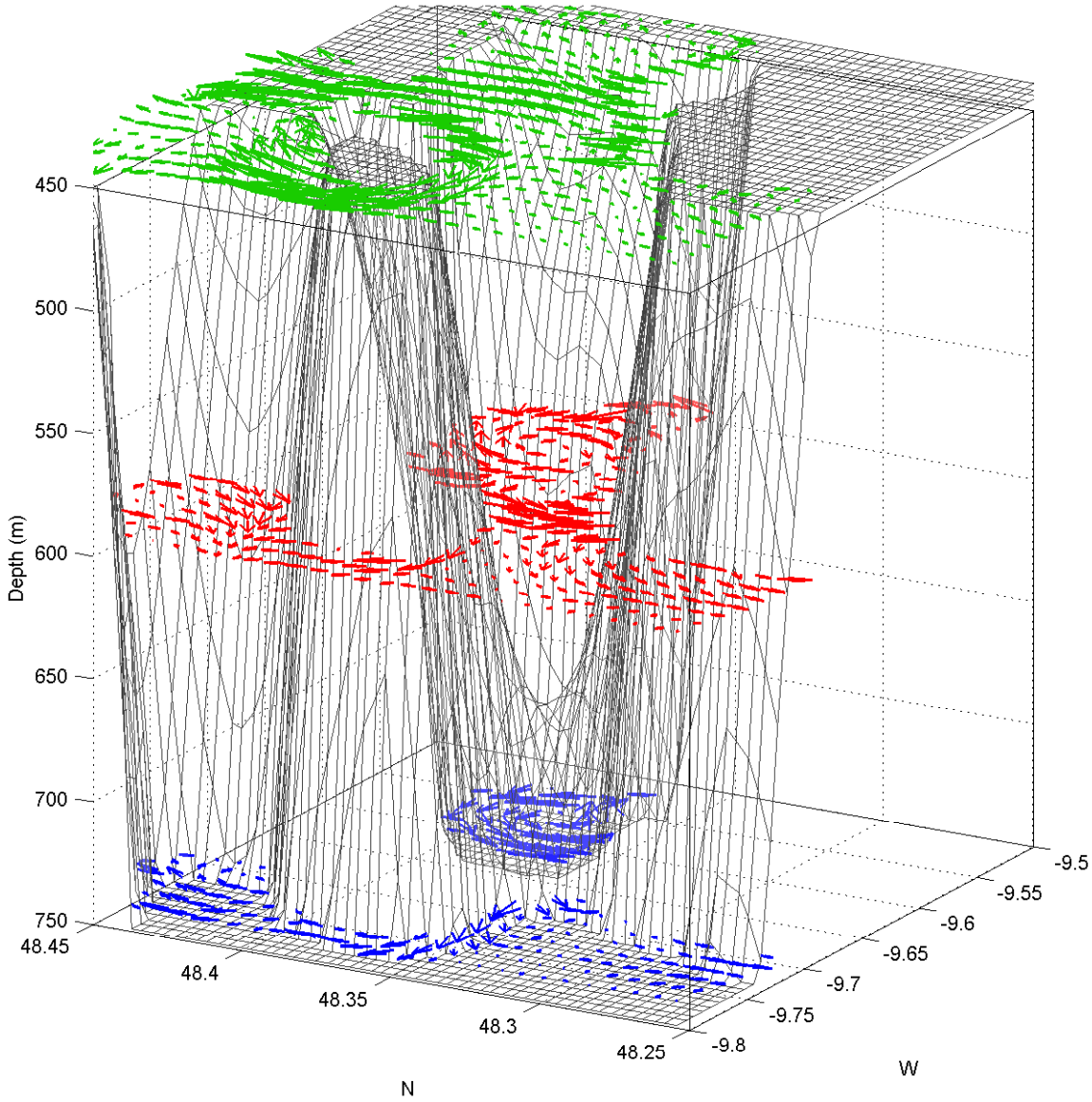

Figure 12. Velocity vectors of the model predicted baroclinic eddy generated inside the canyon. The currents are shown at depths 450 m (green arrows), 600 m (red arrows) and 700 m (blue arrows).

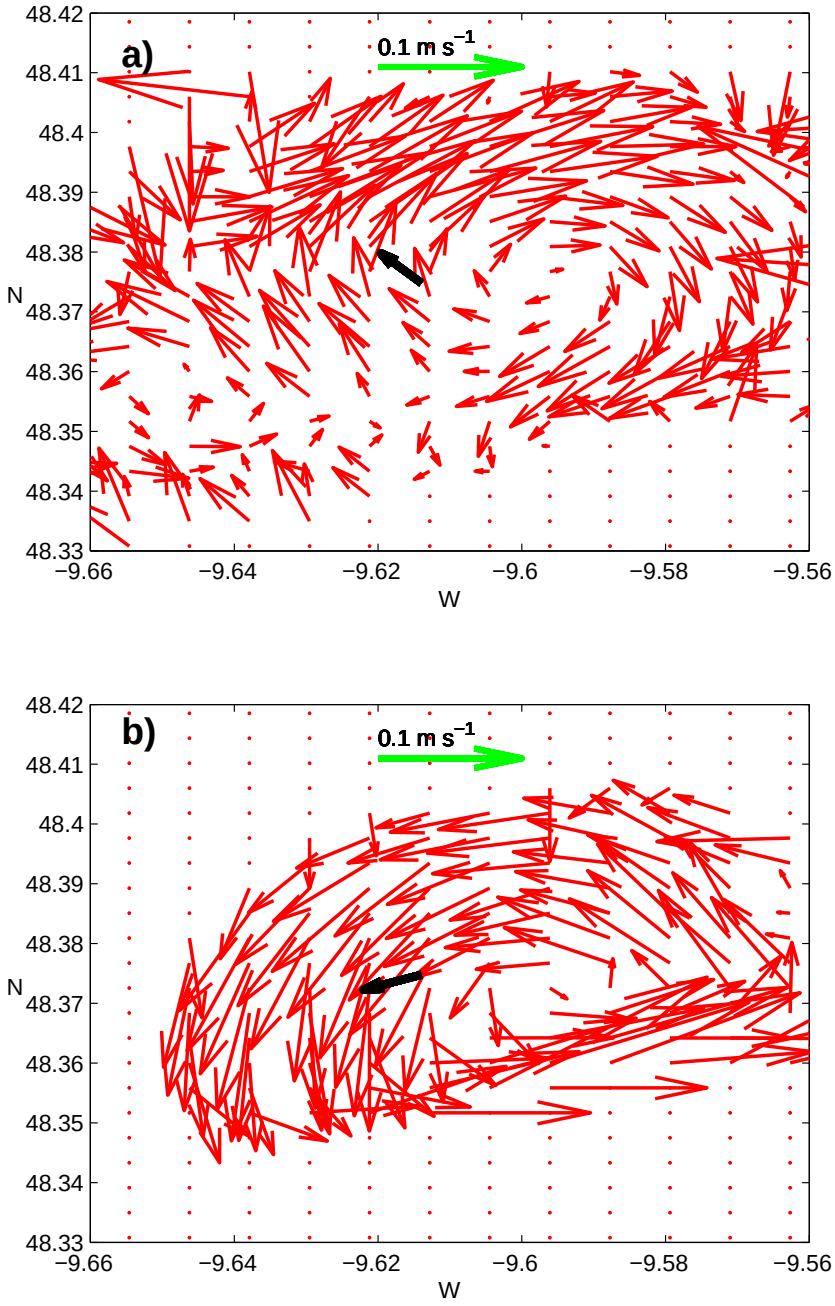

Figure 13. Model predicted anti-cyclonic and cyclonic eddies at the depths of 600 m (a) and 750 m (b). Average baroclinic currents recorded by LADCP at the same depths are shown by black arrows.

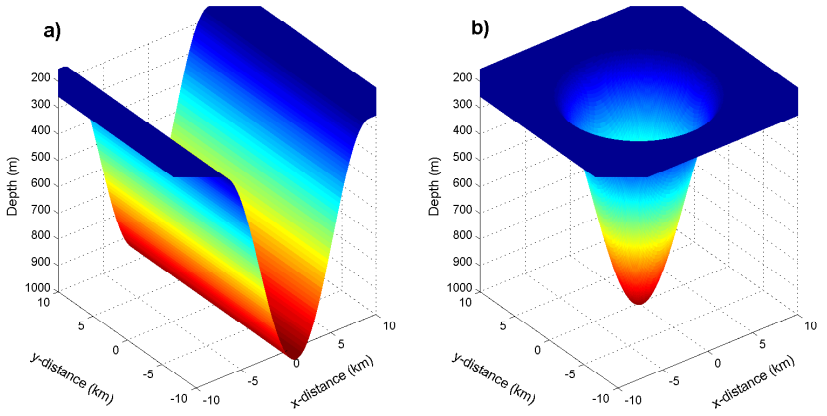

Figure 14. Bottom topography of idealised a) two-dimensional and b) three-dimensional canyons.

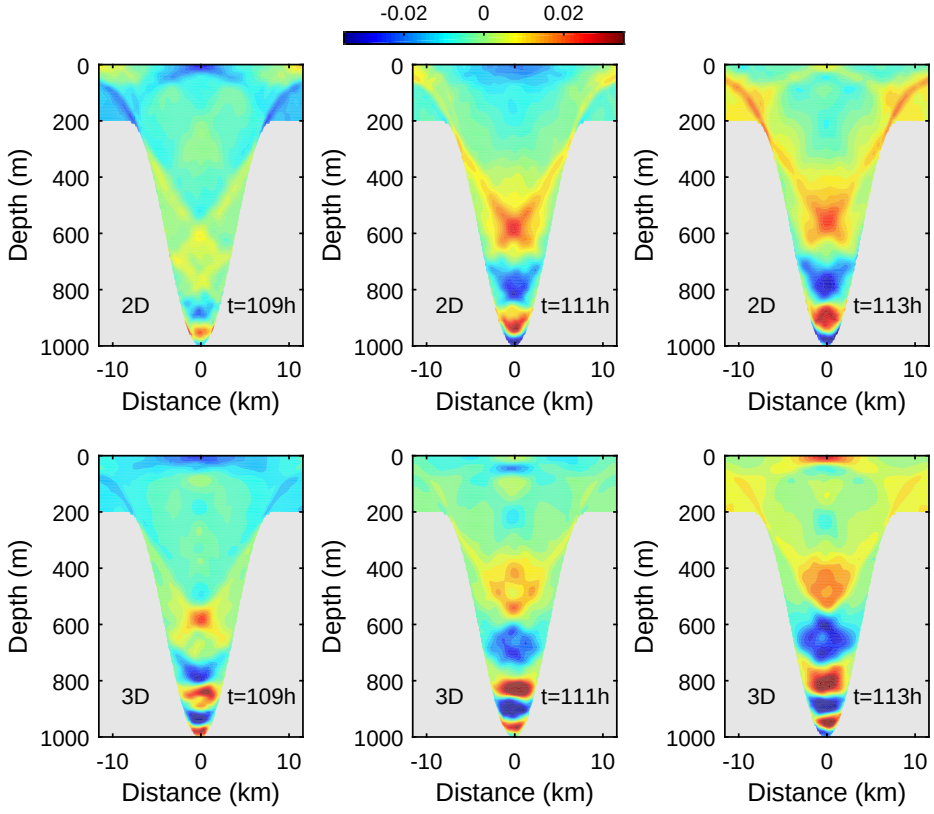

Figure 15. Instant horizontal velocities in the two-dimensional (top panels) and three-dimensional (bottom panels) canyons. The time after beginning of the numerical experiment is shown in the bottom right corner of each panel.

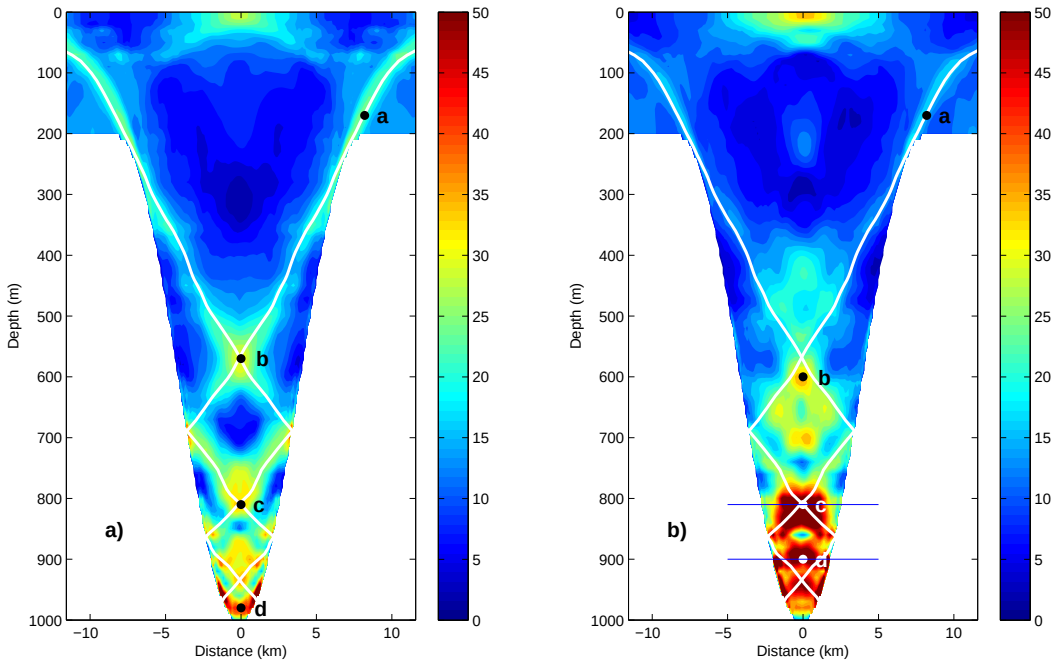

Figure 16. Amplitude of the baroclinic tidal energy (Jm^{-3}) in a) two-dimensional and b) three-dimensional canyons. Dotted white contours depict characteristic lines (1).

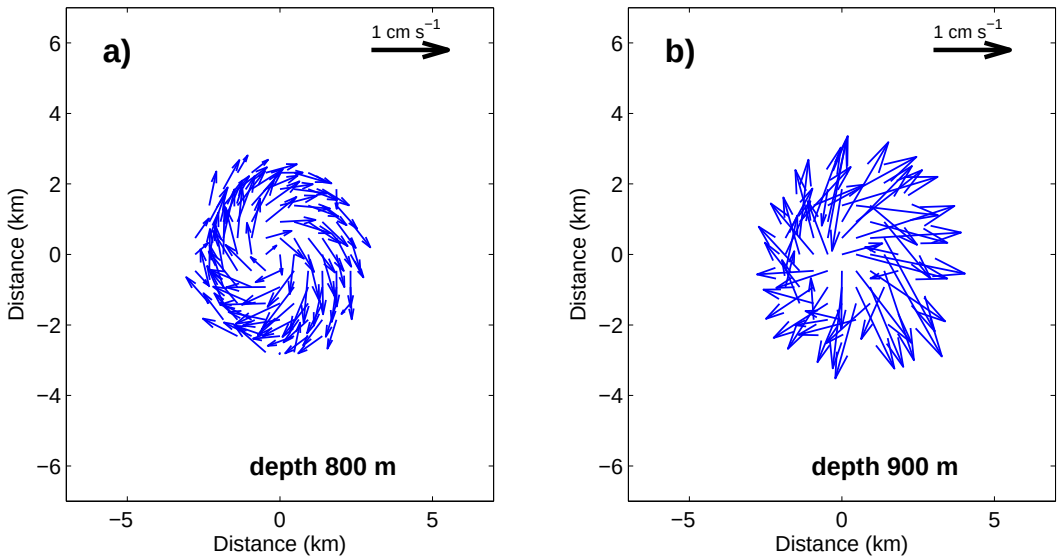

Figure 17. Model predicted anti-cyclonic eddies in an ideal circular canyon.